Composites Part B 263 (2023) 110850

Contents lists available at ScienceDirect

Composites Part B

journal homepage: www.elsevier.com/locate/composites

Towards understanding the role of viscoelasticity in microstructural buckling in soft particulate composites

Yuhai Xiang [a,b], Dean Chen [a], Nitesh Arora [a], Qi Yao [a], Stephan Rudykh [a,c,*]

[a] Department of Mechanical Engineering, University of Wisconsin-Madison, Madison, WI, USA
[b] Department of Chemical Engineering and Materials Science, University of Minnesota, Minneapolis, MN, USA
[c] School of Mathematical and Statistical Sciences, University of Galway, Galway, Ireland

ARTICLE INFO

Keywords:
Particulate composite
Viscoelasticity
Buckling
Critical strain

ABSTRACT

This work investigates the interplay between viscoelasticity and instabilities in soft particulate composites undergoing finite deformation. The composite is subjected to in-plane deformation at various constant strain rates, and experiences microstructural buckling upon exceeding the critical strain level. We characterize the dependence of the critical strain and wavelength on the applied strain rate through our numerical analysis.

In the simulations, we employ the single and multiple-branch visco-hyperelastic models. We find that the critical strain and wavelength – characterized by the single-branch model – show a non-monotonic dependence on the strain rate, reaching a maximum at a specific strain rate. Remarkably, different buckling patterns (with different critical wavelengths) can be activated by changing strain rates. The space of admissible buckling modes widens in composites with higher instantaneous shear modulus. In the composites characterized by the multiple-branch model, the critical strain function exhibit multiple local maxima following a superposition of the single-branch responses. Typically, the branch with a larger relaxation time has a more significant effect on the critical strain. Moreover, the local maximum (of the critical strain function) is amplified by increasing the strain–energy factor of the corresponding branch term.

Finally, we perform the experiments on the 3D-printed particulate soft composite characterized by a broad spectrum of relaxation times. The comparison of the experimental and simulation results demonstrates the ability of the numerical model to predict the critical buckling characteristics.

1. Introduction

Soft microstructured materials are prone to developing elastic instabilities frequently leading to microstructure transformations [1]. In the post-buckling regime, the material can exhibit auxetic behavior [2–4], shape transformations [5], tunable color [6], and tunable bandgaps [7–9]. Moreover, buckling-induced microstructure transformations can be employed to design soft robots [10].

The "small-on-large" framework [11] is frequently used to detect the onset of instabilities. In soft composites, the instabilities can develop at microscopic and macroscopic length scales [12]. The onset of the macroscopic or longwave instability can be detected through the loss of ellipticity analysis requiring the evaluations of the tensor of elastic moduli. The tensor of elastic moduli can be calculated through analytical or numerical micromechanics-based homogenization approaches [13–17] or, alternatively, can be derived from phenomenological models [18–26]. The analysis of microscopic instability requires a more demanding approach and usually employs the Bloch-Floquet method [12]. Triantafyllidis et al. [27] applied the technique to study the instability of the two-phase composite with circular inclusions arranged in a square and a diagonal 2D periodic unit cell with various volume fractions. Lopez-Pamies and Castañeda [28] conducted a study on instabilities in particulate composites with elliptical inclusions undergoing finite deformation. In particular, they examined the impact of varying volume fractions and the initial aspect ratios of the elliptical cross-section of the inclusions on the composite's buckling behavior. Li et al. [29] reported the experimental observations of the numerically predicted instability-induced microstructure transformations in the soft particulate composites. Chen et al. [30] examined the instability in the soft particulate composites with varying configurations of periodically distributed inclusions and reported distinct instability patterns, including strictly doubled periodicity, seemingly nonperiodic states, and longwave patterns, and their development in the postbuckling regime [31]. Arora et al. [32] studied the influence of inhomogeneous interphases on instabilities in laminates. The effect of phase compressibility of the layered materials has been analyzed

---

[*] Corresponding author at: Department of Mechanical Engineering, University of Wisconsin-Madison, Madison, WI, USA.
E-mail address: rudykh@wisc.edu (S. Rudykh).

https://doi.org/10.1016/j.compositesb.2023.110850
Received 13 February 2023; Received in revised form 2 June 2023; Accepted 11 June 2023
Available online 20 June 2023
1359-8368/© 2023 The Author(s). Published by Elsevier Ltd. This is an open access article under the CC BY license (http://creativecommons.org/licenses/by/4.0/).

by Li et al. [7]. More recently, Li et al. [33] reported the experimental observations of instability-driven domain formations in soft laminates. They investigated the buckling behavior of particulate composites with varying geometrical configurations. Rudykh and Debotton [15] analyzed the macroscopic instabilities in 3D fiber composites. The series of works [34–38] investigated the microscopic instability and associated buckling modes in deformable 3D fiber composites.

Most theoretical and numerical studies examined the instability phenomenon in purely elastic or hyperelastic materials. However, soft materials exhibit inelastic behavior, including the intrinsic viscoelasticity phenomenon [39–44]. To address the complexity of the inelastic phenomenon, various linear and nonlinear models have been proposed — reviewed by Wineman [45], and more recently by Xiang et al. [46], focusing on physically-based models. In the context of microstructural bucking in soft composites, as we shall show, the viscoelasticity plays an important role, especially in the loading regimes activating the time-dependent mechanisms. Previously, Alur and Meaud [47] performed a numerical study of the rate-dependent behavior of the viscoelastic laminates with a stiff elastic layer and soft viscoelastic matrix. Slesarenko and Rudykh [48] reported the experimental observation of the tunability of wavy patterns in soft viscoelastic laminates. However, little is known about the interplay between viscoelasticity and the instability phenomenon in soft composites.

In this study, we examine the role of viscoelasticity in the instabilities in the soft particulate composite. Section 4 summarizes the numerical results, illustrating the dependence of the buckling characteristics on loading rates for the soft composite described by (i) a single-branch and (ii) multiple-branch visco-hyperelastic models. Finally, in Section 5, the applicability of the multiple-branch visco-hyperelastic model is illustrated in comparison with the experimental results for the 3D-printed soft particulate composites.

2. Theoretical background

A material point of a continuum solid in the undeformed configuration O_0 can be identified with its position vector $\boldsymbol{X}$. After deformation, $\boldsymbol{X}$ will be mapped into the deformed configuration O at the current time t with the corresponding position vector $\boldsymbol{x} = \chi(\boldsymbol{X}, t)$. The deformation gradient $\mathbf{F}$ is defined as $\mathbf{F} = \partial \boldsymbol{x}/\partial \boldsymbol{X}$, and its determinant is $J = \det\mathbf{F} > 0$.

For hyperelastic material, the behavior can be described by a strain energy density function W_H, and the second Piola-Kirchhoff stress $\mathbf{S}_H$ can be obtained by

$$\mathbf{S}_H = 2\frac{\partial W_H}{\partial \mathbf{C}}, \tag{1}$$

where $\mathbf{C} = \mathbf{F}^T\mathbf{F}$ is the right Cauchy-Green deformation tensor. For incompressible hyperelastic material ($J = 1$), Eq. (1) is rewritten as

$$\mathbf{S}_H = 2\frac{\partial W_H}{\partial \mathbf{C}} - p\mathbf{C}^{-1}, \tag{2}$$

where p is an unknown Lagrange multiplier.

For visco-hyperelastic material, we consider a model (Holzapfel [49]) based on the rheological representation of the generalized Maxwell model (schematically illustrated in Fig. 1). The corresponding strain energy density function W_V is

$$W_V = W_\infty + \sum_{\alpha=1}^{M} W_\alpha, \tag{3}$$

where W_∞ characterize the equilibrium state as $t \to \infty$, $W_\alpha = \beta_\alpha W_\infty$ represents the strain energy density function characterizing the non-equilibrium response; this corresponds to the non-linear spring in αth branch; here, β_α is the strain-energy factor that can be used to characterize the value of the instantaneous shear modulus of the αth branch (Holzapfel [49]). The second Piola-Kirchhoff stress $\mathbf{S}_\mathrm{V}$ is

$$\mathbf{S}_V = 2\frac{\partial W_V}{\partial \mathbf{C}} = \mathbf{S}_\infty + \sum_{\alpha=1}^{M} \mathbf{Q}_\alpha, \tag{4}$$

where $\mathbf{S}_\infty$ is the equilibrium stress and $\mathbf{Q}_\alpha$ is the non-equilibrium stress of the αth branch. The equilibrium stress $\mathbf{S}_\infty$ is

$$\mathbf{S}_\infty = 2\frac{\partial W_\infty}{\partial \mathbf{C}} - p_\infty \mathbf{C}^{-1}, \tag{5}$$

where p_∞ is an unknown Lagrange multiplier. The non-equilibrium stress $\mathbf{Q}_\alpha$ is calculated through the evolution equation as

$$\dot{\mathbf{Q}}_\alpha + \frac{\mathbf{Q}_\alpha}{\tau_\alpha} = \beta_\alpha \dot{\overline{\mathrm{Dev}(\mathbf{S}_\infty)}}, \tag{6}$$

where τ_α is the relaxation time of the αth branch, $(\dot{\blacksquare})$ is the time derivative and $\mathrm{Dev}\,(\blacksquare) = (\blacksquare) - 1/3\,[(\blacksquare) : \mathbf{C}]\,\mathbf{C}^{-1}$ is the deviatoric operator.

The strain energy density function W_r ($r = H, \infty, \alpha$) of isotropic material can be expressed in terms of the invariants of the right Cauchy-Green tensor as

$$W_r = W_r\left(I_1, I_2, I_3\right) \tag{7}$$

where

$$I_1 = \mathrm{tr}\mathbf{C}, \quad I_2 = \frac{1}{2}\left[(\mathrm{tr}\mathbf{C})^2 - \mathrm{tr}\mathbf{C}^2\right], \quad I_3 = \det\mathbf{C} = J^2 \tag{8}$$

For incompressible materials, $I_3 = 1$. The strain energy density function of isotropic incompressible materials described by the neo-Hookean model is

$$W_r = \frac{\mu_r}{2}\left(I_1 - 3\right), \tag{9}$$

where μ_r is the initial shear modulus. According to Eqs. (2) and (4), the corresponding second Piola-Kirchhoff stress for the hyperelastic and visco-hyperelastic model are

$$\mathbf{S}_H = \mu_H \mathbf{I} - p\mathbf{C}^{-1} \tag{10}$$

and

$$\mathbf{S}_V(t) = \mu_\infty \mathbf{I} - p_\infty \mathbf{C}^{-1} + \sum_{\alpha=1}^{M} \int_0^t \mu_\infty \beta_\alpha \exp\left(\frac{-(t-\tau)}{\tau_\alpha}\right) \times \dot{\overline{\left[\mathbf{I} - \frac{\mathbf{I} : \mathbf{C}(\tau)}{3}\mathbf{C}(\tau)^{-1}\right]}}\, d\tau, \tag{11}$$

respectively. Here, $\mathbf{I}$ is the identity tensor; the corresponding Cauchy ($\boldsymbol{\sigma}$) and first Piola-Kirchhoff ($\mathbf{P}$) stress tensors are related to the second Piola-Kirchhoff stress tensor through $\boldsymbol{\sigma} = J^{-1}\mathbf{FSF}^\mathrm{T}$ and $\mathbf{P} = \mathbf{FS}$, respectively.

3. Finite element simulations

Consider the soft particulate composite consisting of stiff circular inclusions embedded in the soft matrix, as illustrated in Fig. 2. The geometry of the structure is defined through the inclusion spacing ratio $\xi = d_0/h_0$; where h_0 is the height of the primitive unit cell, and d_0 is the diameter of the inclusions.

To analyze the instabilities in the soft composite, we carry out the numerical analysis through finite element simulations in COMSOL 5.6. We use a single-column inclusion system with a large enough number of inclusions ($N = 40$, if not specified otherwise) along $\mathbf{e}_1$-direction in the representative cell (see Fig. 2). We apply the in-plane unidirectional compression by imposing the periodic displacement boundary conditions on the representative cell as

$$\boldsymbol{U}_{AB} - \boldsymbol{U}_{CD} = \left(\overline{\mathbf{F}} - \mathbf{I}\right)\left(\boldsymbol{X}|_{AB} - \boldsymbol{X}|_{CD}\right), \tag{12}$$

$$\boldsymbol{U}_{BD} - \boldsymbol{U}_{AC} = \left(\overline{\mathbf{F}} - \mathbf{I}\right)\left(\boldsymbol{X}|_{BD} - \boldsymbol{X}|_{AC}\right), \tag{13}$$

where $\boldsymbol{U}$ is the displacement vector. The subscript AB, CD, AC, and BD denote the interior node on the top, bottom, left, and right edges of the representative cell, respectively, and the “A”, “B”, “C”, and “D” are illustrated in Fig. 2. To prevent rigid body motion, we impose a

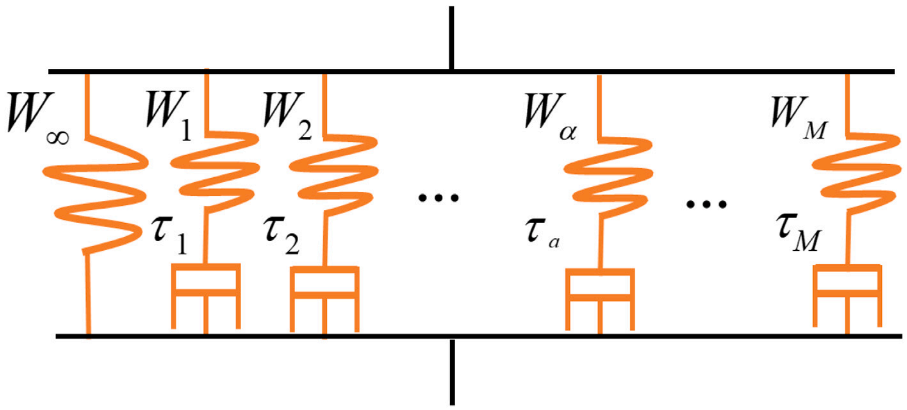

Fig. 1. The rheological representation of the generalized Maxwell model.

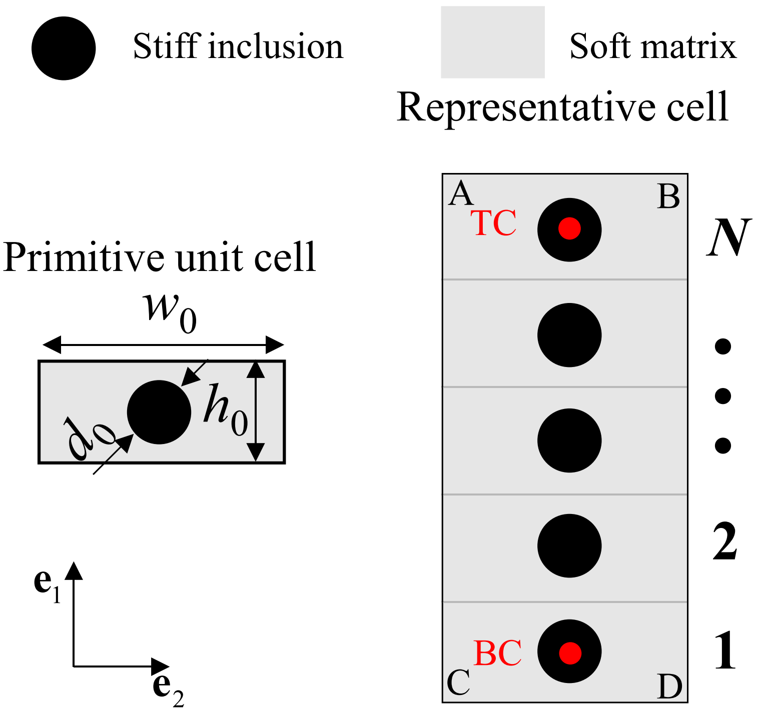

Fig. 2. Schematic illustration of the primitive unit and representative cell. (For interpretation of the references to color in this figure legend, the reader is referred to the web version of this article.)

constraint as $\boldsymbol{U}|_{\mathrm{TC}}+\boldsymbol{U}|_{\mathrm{BC}}=0$. Here the subscript “TC” and “BC” are the center points of inclusions on the top and bottom of the representative cell, respectively (see the red points in Fig. 2). $\overline{\mathbf{F}}$ is the average applied deformation gradient tensor and is expressed as

$$\overline{\mathbf{F}} = \bar{\lambda}\mathbf{e}_1 \otimes \mathbf{e}_1 + \bar{\lambda}^{-1}\mathbf{e}_2 \otimes \mathbf{e}_2 + \mathbf{e}_3 \otimes \mathbf{e}_3, \tag{14}$$

where $\bar{\lambda}(t) = 1 - \varepsilon$ is the applied macroscopic stretch ratio in the compression direction; since the deformation is applied at the constant rate, $\varepsilon = \dot{\varepsilon}t$, with $\dot{\varepsilon}$ being the strain rate.

Here and thereafter, we use superscripts (i) and (m) to represent the stiff inclusions and soft matrix, respectively. The stiff inclusions are modeled by the hyperelastic model and the soft matrix is characterized by the visco-hyperelastic model (as introduced in Section 2). In particular, the neo-Hookean strain energy density function is adopted, namely,

$$W_r^{(q)} = \frac{\mu_r^{(q)}}{2}\left(I_1 - 3\right), \tag{15}$$

where $q = i$ and m, $\mu_H^{(i)}$ denotes the initial shear modulus of the inclusion; $\mu_\infty^{(m)}$ is the initial shear modulus of the equilibrium response of the soft matrix, and $\mu_\alpha^{(m)} = \beta_\alpha \mu_\infty^{(m)}$ is the initial shear modulus of the temporary non-equilibrium response of αth branch of the visco-hyperelastic model (see Eq. (11)).

In our numerical simulation, we focus on composite configuration with weak interactions between columns of inclusions; accordingly, we assign a high unit cell aspect ratio, $w_0/h_0 = 32$. Note that, for purely elastic composites (without the consideration of viscoelasticity), for w_0/h_0 approximately exceeding 6, the influence of the aspect ratio on the critical strain and wavenumber becomes negligible [29]. The inclusion spacing ratio is set as $\xi = 0.8$. The initial equilibrium shear modulus of the matrix $\mu_\infty^{(m)} = 0.1614$ MPa. The contrast between the initial shear modulus of stiff inclusions and the initial equilibrium shear modulus of the matrix is set as $\mu_H^{(i)}/\mu_\infty^{(m)} = 10^5$. Thus, the deformation of stiff inclusions is negligible compared to the soft matrix. Recall that, for the purely elastic composites, the critical strain and wavenumber,

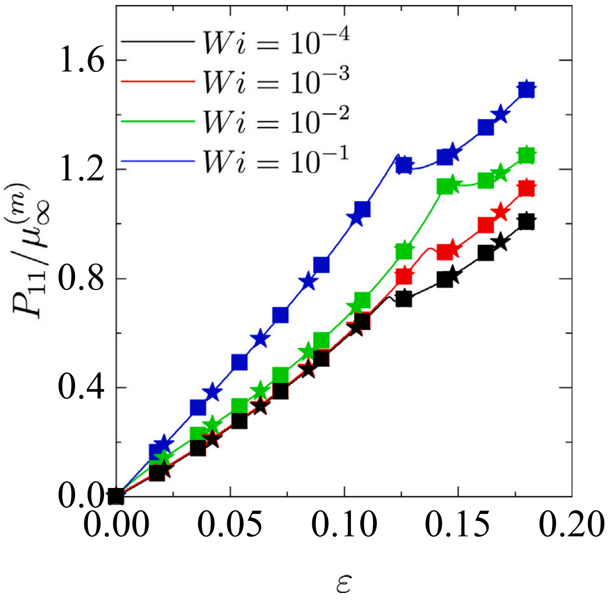

Fig. 3. The dependence of the normalized stress–strain curves on Wi. The solid curve, square and star marks represent the results for τ_1 = 0.1 s, 1 s and 10 s, respectively. (For interpretation of the references to color in this figure legend, the reader is referred to the web version of this article.)

maintain a constant trend when the shear modulus contrast is increased beyond 1000 [29].

4. Results

4.1. Single-branch visco-hyperelastic model

We start by discussing the rate-dependent buckling behavior with the single-branch visco-hyperelastic model. For the single-branch model, there are only two independent parameters: relaxation time τ_1 and strain-energy factor β_1. We study the effect of τ_1 and β_1 on the critical strain and wavelength.

4.1.1. The effect of relaxation time τ_1

Fig. 3 shows the dependence of the normalized stress component $P_{11}/\mu_\infty^{(m)}$ on the applied strain for the composite with $\beta_1 = 1$. The results are shown for different loading regimes characterized by values of the Weissenberg number, $Wi = \dot{\varepsilon}\tau_1$. In particular, the black, red, green, and blue curves and markers represent the mechanical response for composite with the applied loading rates corresponding to $Wi = 10^{-4}$, 10^{-3}, 10^{-2}, and 10^{-1}, respectively. The solid curves, square, and star markers correspond to the results for the composites with τ_1 = 0.1 s, 1 s, and 10 s, respectively. We note that the mechanical response is independent of the relaxation time τ_1 for a given Wi. The same values of Wi indicate that composites experience equivalent loading rates despite being characterized by different relaxation times τ_1. While this behavior can be expected for homogeneous material, in the particulate composite, however, is not apparent since the deformation and the deformation rate vary spatially.

Fig. 4 shows the dependence of the critical strain ε_{cr} (a) and normalized critical wavelength $\bar{l}_{cr}$ (b) on Weissenberg number Wi, and the buckling pattern (c) corresponding to $Wi = 10^{-2}$. We highlighted the critical wavelength for the composite loading with the strain rate corresponding to $Wi = 10^{-2}$ by the red star in Fig. 4(b). The normalized critical wavelength represents the number of inclusions in the repeating set of the buckled shape. The critical strain and wavelength are identified from the stress–strain curve and the buckling pattern, respectively. Specifically, we monitor the macroscopic stress of the composites during the compression, and we identify the strain at which the dependence of stress on strain changes sharply as the critical strain. The discrete Fourier transform (DFT) method is employed to identify the critical wavelength of the buckled composites. Here, the circle, square, and star markers represent the results for the composites with τ_1= 0.1 s, 1 s and 10 s, respectively. The critical strain is a smooth function of the Weissenberg number. We connect the markers with a dotted curve to indicate the rate dependence trend. However, the critical wavelength is not a smooth function of the Weissenberg number, so the connecting curves between the markers show the variation tendency only, not the actual value. High (such as $Wi = 10$) and low loading rates (such as $Wi = 10^{-7}$) can suppress the viscoelasticity. So that we can estimate the critical strain and wavelength for the two extreme cases through the Bloch-Floquet analysis for purely elastic composites [29,37]. The results for the purely elastic composites are denoted by the gray dashed curve in Fig. 4(a) and (b). Note that, due to the high contrast in $\mu_H^{(i)}/\mu_\infty^{(m)}$, the critical strain and wavelength in the two limits (high and low loading rates) are almost identical.

We note that the critical strain and wavelength are identical for the same Wi regardless of τ_1 (compare the different types of markers). Besides, the critical strain approaches the value corresponding to the limits for sufficiently fast (or slow) loading rates. Specifically, ε_{cr} = 0.1123 (for Wi = 10) and ε_{cr} = 0.11198 (for $Wi = 10^{-7}$), approaching the critical value for the elastic composites, ε_{cr} = 0.11078, as calculated through the Bloch-Floquet analysis. Interestingly, for Wi ranging from 10^{-7} to 10, the dependence of the critical strain on Wi is non-monotonic, with the maximum of the critical strain being significantly larger than the values in the two extreme cases. In particular, the peak value of the critical strain is 0.1466, being larger than the critical strain (0.11078) from the Bloch-Floquet analysis (compare the peak value of the black dotted curve and the value of the gray dashed curve in Fig. 4(a)). This composite behavior is different from that observed in the laminated composite, for which the critical buckling strain is a monotonic function of the strain rate bounded by the two limits for sufficiently fast and slow loading rates. For example, in the laminates with viscoelastic matrix (and elastic layers), the critical strain increases with an increase in the applied strain rate [47], and the opposite rate dependence will be observed if the fiber is viscoelastic [48].

We observe that the rate dependence of the critical wavelength is non-monotonic (see Fig. 4(b)), reaching the maximum plateau at a range of intermediate values of Wi. In particular, $\bar{l}_{cr}$ reaches the highest plateau value when Wi is within the range of 10^{-3} to 10^{-2}. For low loading rates, such as $Wi = 10^{-7}$, and high loading rates such as Wi = 10, the critical wavelength reaches the plateau value $\bar{l}_{cr}$ = 4.44 being close to the value from the Bloch-Floquet analysis ($\bar{l}_{cr}$ = 4.56). Recall that the normalized critical wavelength $\bar{l}_{cr}$ represents the number of inclusions in the repeating sets of the instability-induced wavy pattern; therefore, $\bar{l}_{cr}$ might be expected to be an integer. However, a buckling pattern may not attain a perfect periodicity (with an integer number of repeating inclusions), as illustrated in Fig. 4(c), where two alternating sets of six and seven inclusions can be observed. To identify the wavelength of the instability-induced irregular quasi-periodic pattern, we use the discrete Fourier transform (DFT) method. Through the analysis, we determine the dominant wavelength in the instability-induced wavy pattern. Note that the obtained normalized critical wavelength is not always an integer. For example, the DFT dominant wavelength of the composite undergoing deformation at the rate corresponding to $Wi = 10^{-2}$ (shown in Fig. 4(c)) is 6.67; the value is between the two wavelengths with an integer number of inclusions (6 and 7) of the corresponding repeating blocks. We also note that the critical wavelength function is not smooth; with the Weissenberg number increasing from 10^{-7} to 10, the critical wavelength takes the discrete values of 4.44, 5.0, and 6.67, respectively. This observation indicates that different loading rates may activate buckling modes with different wavelengths and the wavelength of the activated modes does not continuously change with an increase in the loading rate.

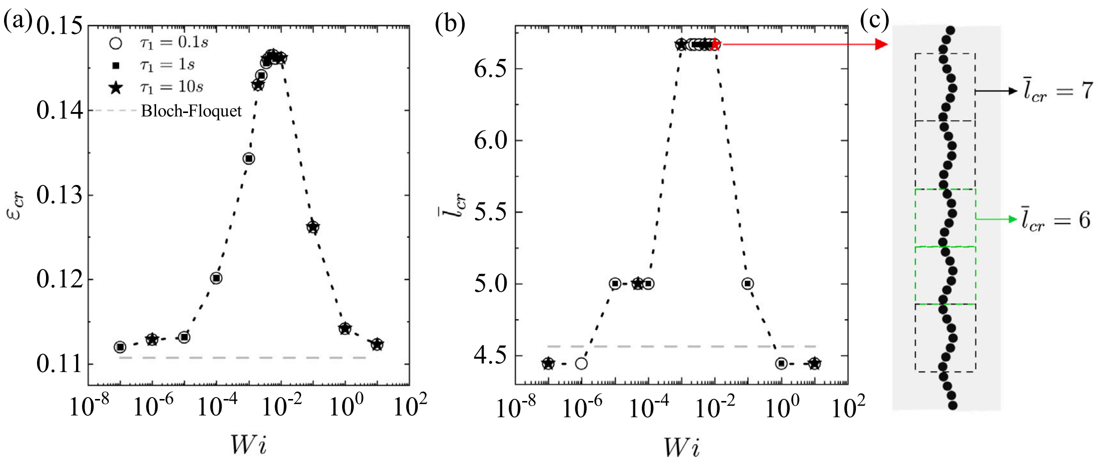

Fig. 4. The dependence of (a) critical strain ε_{cr} and (b) normalized critical wavelength $\bar{l}_{cr}$ on Wi. (c) The buckling pattern corresponds to the red marker in (b). The circle, square, and star marks represent the results for $\tau_1 = 0.1$ s, 1 s and 10 s, respectively.

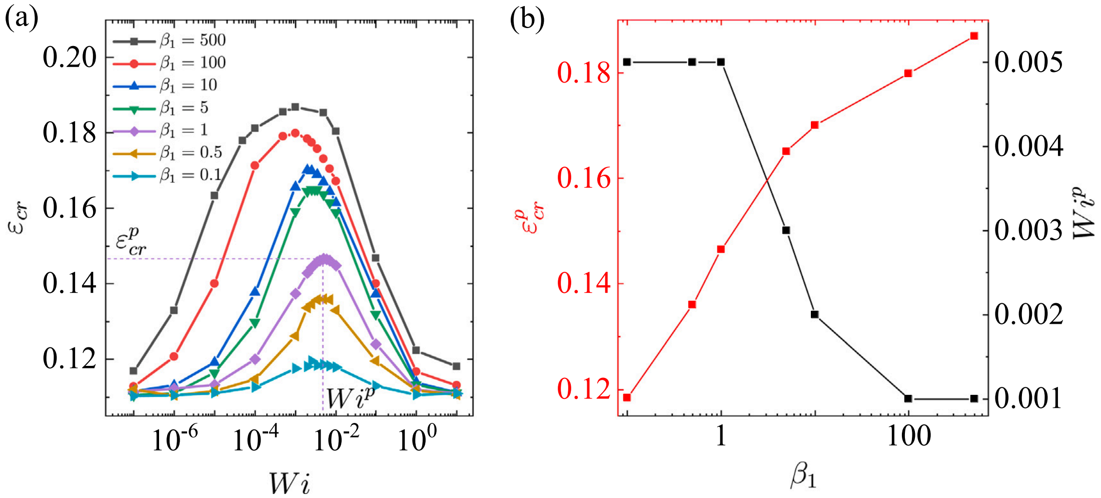

Fig. 5. The dependence of (a) rate-dependent critical strain ε_{cr}, (b) peak point-related critical strain ε_{cr}^p and Weissenberg number Wi^p on β_1. (For interpretation of the references to color in this figure legend, the reader is referred to the web version of this article.)

4.1.2. The effect of the strain-energy factor β_1

To illustrate the influence of the strain-energy factor on the buckling characteristics, we first show the dependence of the critical strain ε_{cr} on the strain-energy factor β_1 in Fig. 5(a). Specifically, we show the rate-dependent critical strain for β_1 changing from 0.1 to 500. For later discussions, let us consider the dependence of the peak point-related critical strain ε_{cr}^p (red curve) and Weissenberg number Wi^p (black curve) on the strain-energy factor (see Fig. 5(b)). Here, ε_{cr}^p is the maximum critical strain and Wi^p is the corresponding Weissenberg number for a given β_1 (ε_{cr}^p and Wi^p for $\beta_1 = 1$ are illustrated by the violet dashed lines in (a)).

We observe that the critical strain shows a similar rate dependence for different β_1, namely, the critical strain increases first, then, after reaching the maximum, it starts decreasing with an increase in Wi. For example, for $\beta_1 = 1$, the critical strain increases until its maximum value reaching $\varepsilon_{cr}^p = 0.1466$ at $Wi^p = 5 \times 10^{-3}$, and then decreases with a further increase in Wi (see the violet curve in (a)). In addition, the critical strain increases with an increase in β_1 (compare the different colored curves in Fig. 5(a)). Fig. 5(b) shows that the peak point of critical strain ε_{cr}^p increases with an increase in β_1. However, Wi^p shows the opposite trend, namely, it decreases with an increase in the strain-energy factor approaching around 5×10^{-3} and 10^{-3} when $\beta_1 \leq 1$ and $\beta_1 \geq 100$. The dependence of the critical strain on the strain-energy factor can be related to the effective modulus contrast of inclusions and matrix. For the hyperelastic particulate composites (in the absence of viscoelasticity), it has been reported that the critical strain monotonically increases with a decrease in the inclusions-to-matrix shear modulus contrast [29]. In visco-hyperelastic materials, the effective modulus of the matrix increases with an increase in β_1. Therefore, the modulus contrast between inclusions and matrix is lower for composites with a larger strain-energy factor for a given loading rate. As a result, the corresponding critical strain increases with an increase of β_1. The rate and the strain-energy factor dependence of critical strain can guide us to design the particulate composite. For instance, to make a more stable particulate composite, we could make the matrix material with a larger strain-energy factor. In addition, for composite undergoing the specified strain rate, we could adjust the relaxation time of the matrix material to restrict the Weissenberg number to the intermediate range where the composite is more stable.

Fig. 6 shows the dependence of the normalized critical wavelength $\bar{l}_{cr}$ on Weissenberg number Wi. The results are shown for the composites with various strain-energy factor values β_1 (from 0.1 to 500). Similar to the previous observations, here, we also find that $\bar{l}_{cr}$ is not a smooth function of the Weissenberg number, and it only switches between values $4.44,\ 5.0,\ 5.71,\ 6.67,$ and 10 with a change in Wi. We observe that slow (such as $Wi = 10^{-7}$) and fast (such as $Wi = 10$) loading rates limit the appearance of possible buckling modes. In

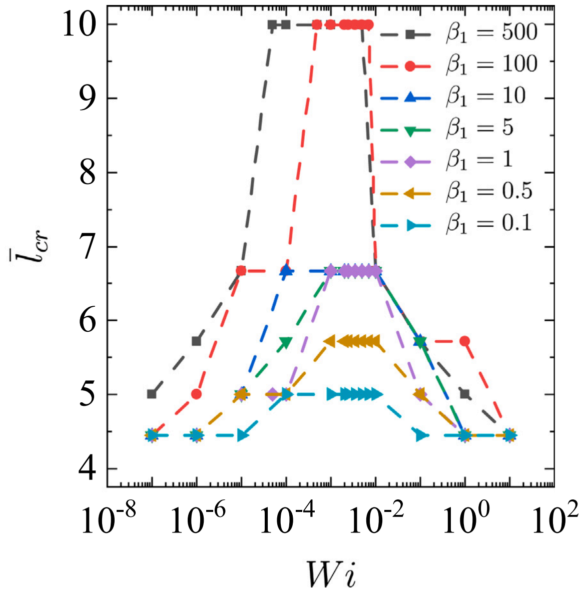

Fig. 6. The dependence of normalized critical wavelength $\bar{l}_{cr}$ on Weissenberg number Wi for composites with various strain-energy factor β_1. (For interpretation of the references to color in this figure legend, the reader is referred to the web version of this article.)

particular, $\bar{l}_{cr}$ shifts between 4.44 and 5.0 only for $Wi = 10^{-7}$, and takes a single value of 4.44 for $Wi = 10$ over a range of β_1 (from 0.1 to 500).

In addition, we note that $\bar{l}_{cr}$ shows an increasing trend with an increase in β_1 for composites with strain-energy factors smaller than 100. The normalized critical wavelength can span a broader range of values with the change of Wi for higher β_1. For example, $\bar{l}_{cr}$ has two possible values for $\beta_1 = 0.1$ (see the light blue curve), three possible values for $\beta_1 = 0.5$ and 1 (see the brown and violet curves), four possible values for $\beta_1 = 5$ and 10 (see the green and dark blue curves), and five possible values for $\beta_1 = 100$ and 500 (see the red and black curves). We can conclude that overall a broader set of possible buckling modes can be activated in composites characterized by higher strain-energy factors. Therefore, to obtain a particulate composite with wider space admission of the buckling pattern activated by different strain rates, we could select matrix material with a larger strain-energy factor.

4.2. Multiple-branch visco-hyperelastic model

In this section, we examine the rate sensitivity of the critical strain in the composite with the matrix characterized by the multiple-branch visco-hyperelastic model. Fig. 7 shows the dependence of critical strain on strain rate for the composites with matrix described by the double-branch model (corresponding to $M = 2$ in Eq. (11)). The results are shown for the composites with $\beta_1 = \beta_2 = 0.5$, and $\tau_1 = 1$ s and $\tau_2 = 100$ s in Fig. 7(a); and for the case of $\beta_1 = \beta_2 = 0.5$, and $\tau_1 = 0.01$ s and $\tau_2 = 10$ s in Fig. 7(b). The continuous and dashed curves represent the results for the double-branch and single-branch models, respectively. The single branch models are characterized by their corresponding strain-energy factor and relaxation times: $\beta_1 = 0.5$, $\tau_1 = 1$ s (the black dashed curve) and $\beta_2 = 0.5$, $\tau_2 = 100$ s (the red dashed curve) in Fig. 7(a); and $\beta_1 = 0.5$, $\tau_1 = 0.01$ s (the black dashed curve) and $\beta_2 = 0.5$, $\tau_2 = 10$ s (the red dashed curve) in Fig. 7(b).

We observe that the critical strain function is characterized by two local maxima (or two peaks) for both cases. Interestingly, the strain rate values (corresponding to the maxima) coincide with those of the single-branch models with corresponding relaxation times. For example, $\dot{\epsilon}^{p(1)}$ and $\dot{\epsilon}^{p(2)}$ in Fig. 7(a) is the strain rate corresponding to peaks for the composite with the single-branch model with $\beta_1 = 0.5$, $\tau_1 = 1$ s and $\beta_2 = 0.5$, $\tau_2 = 100$ s, respectively (see the vertical dashed gray lines). We also observe that the peak corresponding to the larger relaxation time is higher than the peak corresponding to the shorter relaxation time. In particular, the critical strain is higher for the value corresponding to $\dot{\epsilon}^{p(2)}$ than the value corresponding to $\dot{\epsilon}^{p(1)}$ (see the blue curves). This observation indicates that for the double-branch model having identical strain-energy factors ($\beta_1 = \beta_2$), the branch with a larger relaxation time plays a dominant role in the determination of the critical buckling strain.

Fig. 8 displays the dependence of the critical strain on strain rate for the composites with the matrix characterized by the three-branch model ($M = 3$ in Eq. (11)) in Fig. 8(a), and the five-branch model ($M = 5$ in Eq. (11)) in Fig. 8(b). In Fig. 8(a), we show the results for the three-branch model with two cases: $\beta_1 = \beta_2 = \beta_3 = 1$ as well as $\tau_1 = 0.01$ s, $\tau_2 = 1$ s and $\tau_3 = 100$ s (see the blue curve); $\beta_1 = 10$ and $\beta_2 = \beta_3 = 1$ as well as $\tau_1 = 0.01$ s, $\tau_2 = 1$ s and $\tau_3 = 100$ s (see the violet curve). In Fig. 8(b), we study the five-branch model with $\beta_1 = \beta_2 = \beta_3 = \beta_4 = \beta_5 = 1$ as well as $\tau_1 = 0.01$ s, $\tau_2 = 0.1$ s, $\tau_3 = 1$ s, $\tau_4 = 10$ s and $\tau_5 = 100$ s (see the pink curve). All the dashed curves denote the results of the single-branch model with the corresponding strain-energy factor and relaxation time. For instance, the red, gray, and green dashed curves in Fig. 8(a) denote the results for the composites with $\beta_1 = 1$ and $\tau_1 = 0.01$ s, $\beta_2 = 1$ and $\tau_2 = 1$ s, and $\beta_3 = 1$ and $\tau_3 = 100$ s, respectively.

Note that the values of the strain rate $\dot{\epsilon}^{p(\alpha)}$ ($\alpha = 1$, 2, and 3) corresponding to the maxima coincide with those of the single-branch models with corresponding relaxation times. In particular, $\dot{\epsilon}^{p(\alpha)}$ is the strain rate corresponding to peaks for the composite described by the single-branch model with β_α and τ_α (see the vertical green, gray, and red dashed lines in Fig. 8(a)). Similar to the double-branch model, the magnitude of the peak corresponding to the shorter relaxation time is also lower for the three-branch model. In particular, the critical strain corresponding to $\dot{\epsilon}^{p(1)}$ is lower than the value corresponding to $\dot{\epsilon}^{p(2)}$ (compare the corresponding vertical red and gray dashed lines) and the critical strain corresponding to $\dot{\epsilon}^{p(2)}$ is lower than the value corresponding to $\dot{\epsilon}^{p(3)}$ (compare the vertical gray and green dashed lines).

In addition, we note that the peak of critical strain increases as the corresponding strain-energy factor increases. For example, the peak corresponding to $\dot{\epsilon}^{p(1)}$ increases from 0.11 to 0.16 when we increase β_1 from one to ten (compare the violet and blue curves in Fig. 8(a)). On the contrary, the corresponding strain rate ($\dot{\epsilon}^{p(1)}$) slightly decreases with an increase in β_1 (compare the vertical violet and red dashed lines). The results indicate that for a given branch, a higher strain-energy factor β_α can increase the local peak (determined by this branch) and decrease the strain rate (corresponding to the local peak). These observations are consistent with the numerical results of the single-branch model. For the single-branch model, the maximum critical strain and the corresponding strain rate increase and decrease with an increase in the strain-energy factor, respectively (see the discussion of Fig. 5(b)). Moreover, we find that the increase in the strain-energy factor β_α eliminates its adjacent local peak. In particular, the local peak corresponding to $\dot{\epsilon}^{p(2)}$ disappears when β_1 increases from one to ten (see the violet curve in Fig. 8(a)).

For the five-branch model, we observe that there is a single peak only (see the pink curve in Fig. 8(b)), and the values of the strain rate $\dot{\epsilon}^{p}$ corresponding to the maximum almost coincides with that of the single-branch model with the largest relaxation time ($\tau = 100$ s). These observations indicate that, in the multiple-branch model with identical strain-energy factors, the peaks of critical strain corresponding to larger relaxation time is higher. As a result, the peak (corresponding to the largest relaxation time) is the sharpest and even makes other peaks indiscernible. Therefore, only one peak appears and the corresponding strain rate $\dot{\epsilon}^{p}$ is dictated by the largest relaxation time.

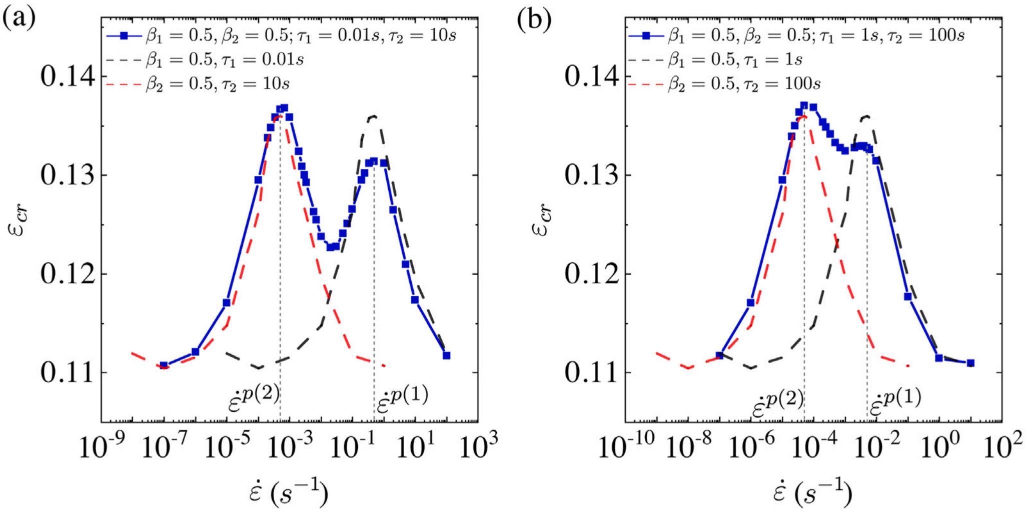

Fig. 7. The dependence of critical strain on strain rate for the composites with matrix characterized by double-branch model with (a) $\tau_1 = 1$ s and $\tau_2 = 100$ s, (b) $\tau_1 = 0.01$ s and $\tau_2 = 10$ s. The strain-energy factors are $\beta_1 = \beta_2 = 0.5$. (For interpretation of the references to color in this figure legend, the reader is referred to the web version of this article.)

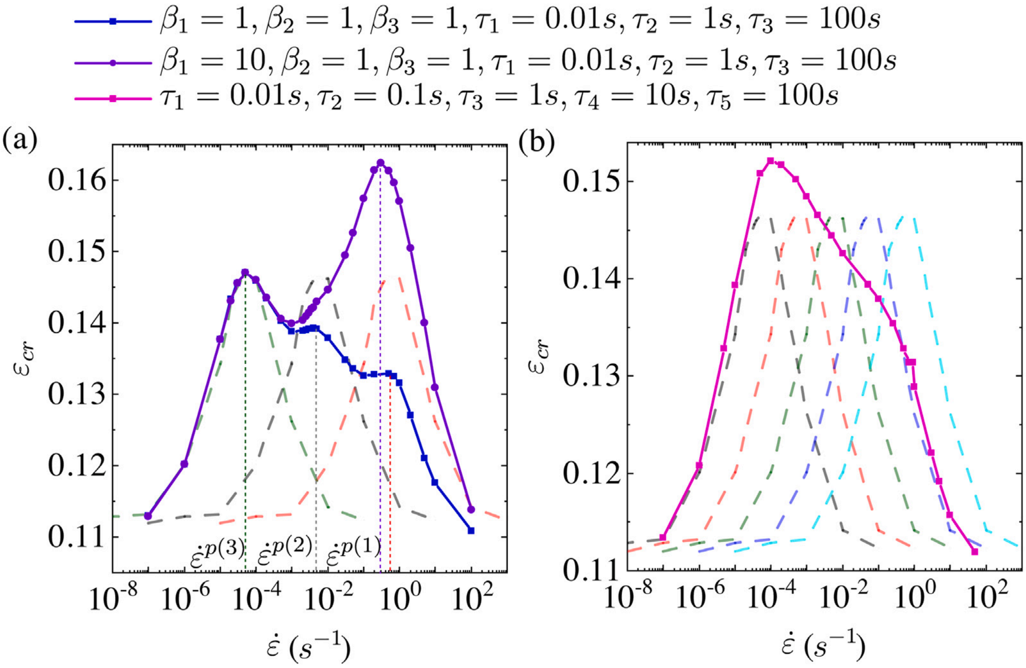

Fig. 8. The dependence of the critical strain on strain rate for the composites with matrix characterized by (a) the three-branch model and (b) the five-branch model. (For interpretation of the references to color in this figure legend, the reader is referred to the web version of this article.)

5. Application of multiple-branch model for 3D-printed soft particulate composite

In this section, we apply the multiple-branch model to capture the instability behavior of the 3D-printed soft particulate composite. To model the 3D-printed soft particulate composite characterized by a broad spectrum of relaxation times [48,50–53], we adopt the multiple-branch visco-hyperelastic model.

The composite samples are fabricated with the help of the Objet Connex 260 3D printer. The dimensions of the specimens are 80 mm × 60 mm (width × height) with 6 mm thickness in the out-plane direction. We examine the composites with a single column of inclusions with the spacing ratio $\xi = 0.8$. The height of the primitive unit cell and the diameter of the inclusions are 2.5 mm and 2 mm, respectively. The soft matrix and stiff inclusions are printed with TangoPlus and VeroBlack, respectively. The stiff inclusions are modeled by incompressible neo-Hookean materials with $\mu_H^{(i)}/\mu_\infty^{(m)} = 10^3$. Based on the dynamic mechanical analysis (DMA) characterization data [54], the TangoPlus material is modeled by the multiple-branch visco-hyperelastic model with $M = 10$ in Eq. (11). The identified material parameters for the matrix (3D printed in TangoPlus) are provided in Appendix.

The in-plane compression tests are carried out by the MTS compression machine at room temperature around 21 °C. The deformation in the thickness direction is restricted by a transparent fixture. The compression is applied at different strain rates: $\dot{\varepsilon} = 10^{-3}$ s^{-1}, 5×10^{-3} s^{-1}, 10^{-2} s^{-1}, 5×10^{-2} s^{-1}, and 10^{-1} s^{-1}. At least four samples are tested for each strain rate.

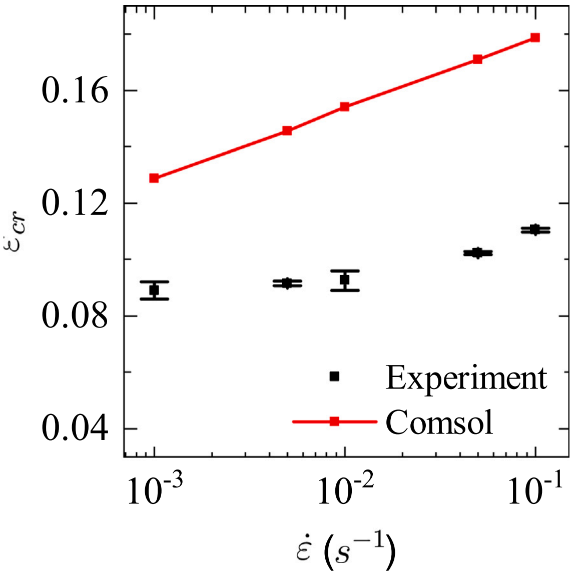

Fig. 9. The dependence of critical strain on applied strain rate for the single column composite system.

Fig. 9 shows the dependence of the critical strain on the applied strain rate. In particular, the experimental (the black makers) and numerical (the red curve) critical strain is presented. The critical strain increases with an increase in the strain rate (within the considered loading range). Our simulations also show a similar trend capturing the rate-dependent behavior qualitatively. We note that, here, the critical strain monotonically increases with an increase in the applied strain rate.

Fig. 10 illustrates the post-buckling patterns observed in experiments (a) and (b), and in simulations (c) and (d). The composite is subject to a compressive strain of 20% with strain rates $\dot{\varepsilon} = 10^{-3}\ \mathrm{s}^{-1}$ (see (a) and (c)) and $\dot{\varepsilon} = 10^{-1}\ \mathrm{s}^{-1}$ (see (b) and (d)). In experiments, we observe that the critical wavelength increases with an increase in the applied strain rate; for example, the normalized critical wavelengths increases from $\bar{l}_{cr} = 6$ to 8 when the strain-rate is increased from $\dot{\varepsilon} = 10^{-3}\ \mathrm{s}^{-1}$ to $10^{-1}\ \mathrm{s}^{-1}$ (see Fig. 10(a) and (b), respectively). Our simulations also predict a similar increase in the critical wavelength, as illustrated in (c) and (d). The numerical prediction of the normalized critical wavelengths for $\dot{\varepsilon} = 10^{-3}\ \mathrm{s}^{-1}$ and $10^{-1}\ \mathrm{s}^{-1}$ are $\bar{l}_{cr} = 5$ and 8, respectively.

We note that the modeling overestimates the critical strain (see Fig. 9), and the predicted post-buckling patterns do not perfectly match the experimental observations. The numerical wavelength is shorter than the observed in the experiment in the composites subjected to $\dot{\varepsilon} = 10^{-3}\ \mathrm{s}^{-1}$; also, the predicted buckling amplitude is visibly lower than that of the experimental pattern, compare, for example, the numerical (b) and experimental (d) results for the case $\dot{\varepsilon} = 10^{-1}\ \mathrm{s}^{-1}$ for the same compressive strain level, 20% (see Fig. 10). The difference between the numerical and experimental results may be attributed to a number of factors, including, possible damage occurring in materials during deformation [46,55,56], friction in the experiment setup, and material properties uncertainties, for example, the material parameters are extracted from the DMA that characterize the material properties in the small deformation range. In the experiments, however, the composite experience high-level deformations (especially the matrix material in the area between the inclusions). A potential way to improve the accuracy of the modeling is the usage of richer constitutive models [46] for the equilibrium and instantaneous responses of the matrix material. Additionally, it is important to note that even under constant environmental temperature, local temperature within the composites might increase due to the viscoelastic behavior of the materials. Therefore, thermo-viscoelastic models could be required to improve the simulation's accuracy [53,57]. We shall mention the existence of the interphases potentially influencing the instability phenomenon in soft composites [32]. Furthermore, the composite buckling behavior may be affected by the imperfections or uncertainties in materials [58–60] or geometry [61–63] of the composites. The influence of uncertainties can be quantified and implemented into the numerical framework through stochastic analysis [64,65].

6. Concluding remarks

We examined the buckling phenomenon in soft particulate composite with the matrix exhibiting by visco-hyperelastic behavior. We started by considering the dependence of the critical strain and wavelength on the applied strain rate in the composite with the matrix characterized by the *single*-branch visco-hyperelastic model. The stress–strain response of the composites (subjected to compression with a constant strain rate) is identical for a given Weissenberg number (regardless of the relaxation time), remarkably, in both stable and post-buckling regimes. While this behavior is expected for homogeneous materials, its appearance in the heterogeneous composites characterized by non-homogeneous local deformation history is noteworthy. The single-branch model predicts the dependence of critical strain on strain rate to have a single prominent maximum. In particular, the composite is more stable at a specific intermediate Weissenberg number and becomes less stable when loaded at smaller and higher strain rates. Based on this, we could make the composites under the given scope of loading rates more stable by restricting the applied Weissenberg number to the intermediate magnitude through adjusting the relaxation time. The Weissenberg number (corresponding to the peak of critical strain) sightly decreases with an increase in the strain-energy factor (or instantaneous shear modulus). The dependence of the critical strain on the strain-energy factor can be interpreted in terms of inclusion-to-matrix shear modulus contrast as follows. The instantaneous shear modulus of the matrix increases with an increase in the strain-energy factor. As a result, the instantaneous inclusion-to-matrix shear modulus contrast decreases with an increase in the strain-energy factor. Li et al. [29] reported that the critical strains in the corresponding hyperelastic particulate system increase with a decrease in the inclusion-to-matrix shear modulus contrast. Therefore, the critical strain shows an increasing trend with an increase in the strain-energy factor. However, the simplified instantaneous-modulus-contrast-based analysis has a limited applicability, and cannot predict the decrease of the critical strain rate in the range of higher strain rates. This regime activates the strong viscoelastic effects amplified by the complexity of spatial inhomogeneity of deformation (and rate of deformation, and its history).

Next, we further examined the buckling phenomenon in the composites with the matrix characterized by a *multiple*-branch visco-hyperelastic model. The critical strain function of the M-branch model tends to posses an M number of local maxima (peaks). The strain rates corresponding to the local maxima are dictated by the single-branch models with the corresponding relaxation times. The branch with the larger relaxation time have a more significant influence on the curve shape, and can eliminate the other peaks (corresponding to the shorter relaxation times). The local maximum can be significantly amplified by increasing the corresponding strain-energy factor. Thus, the branches with larger strain-energy factors have stronger influence on the dependence of the critical strain on strain-rate.

Finally, we experimentally studied the microstructural buckling of the 3D-printed soft particulate composite. The 3D printed matrix material (TangoPlus) used in experiments is characterized by a broad spectrum of relaxation times. Therefore, the multiple-branch visco-hyperelastic model is adopted in numerical simulations for the corresponding matrix. The experimentally observed critical strain and wavelength were found to increase with an increase in the applied

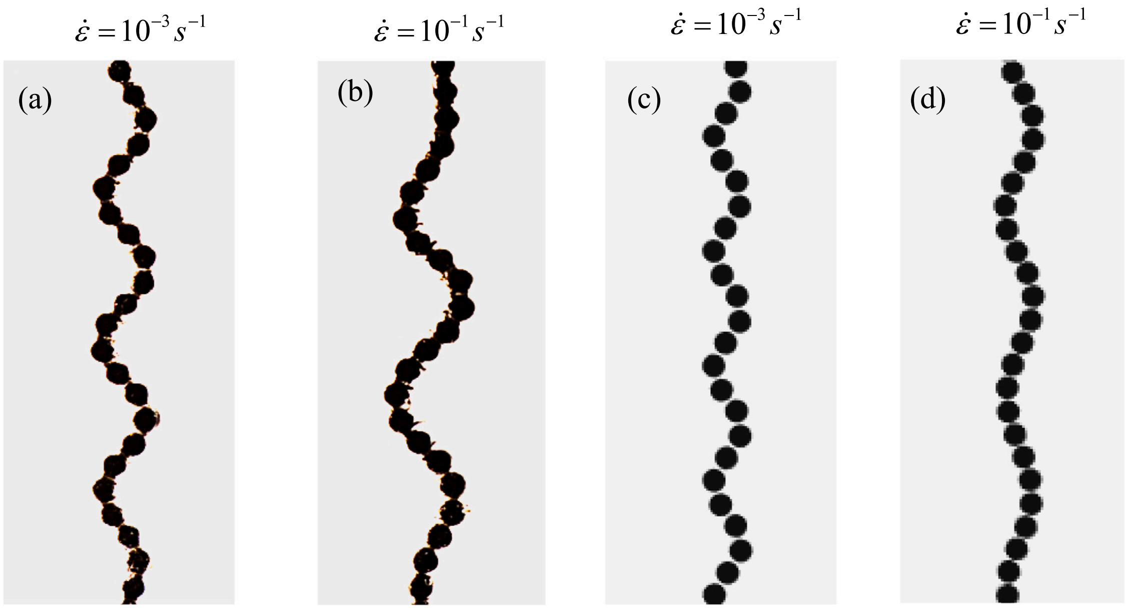
$\dot{\varepsilon} = 10^{-3} s^{-1}$
$\dot{\varepsilon} = 10^{-1} s^{-1}$
$\dot{\varepsilon} = 10^{-3} s^{-1}$
$\dot{\varepsilon} = 10^{-1} s^{-1}$
(a)
(b)
(c)
(d)

Fig. 10. (a) Experimental bucking pattern with (a) $\dot{\varepsilon} = 10^{-3}$ s^{-1} and (b) $\dot{\varepsilon} = 10^{-1}$ s^{-1}. The simulated bucking pattern with (c) $\dot{\varepsilon} = 10^{-3}$ s^{-1} and (d) $\dot{\varepsilon} = 10^{-1}$ s^{-1} for compressive strain 20%.

strain rate; the simulations with the multiple-branch visco-hyperelastic material model can qualitatively capture the dependence of critical strain and wavelength in the complex material system.

Our results provide insights into the complex role of viscoelasticity in the buckling behavior of soft composites. The information can be helpful for the design of soft metamaterials with tunable functions. In particular, the instabilities combined with viscoelasticity can be used to design metamaterials with novel properties that pure elastic metamaterials cannot achieve. For example, viscoelastic metamaterials can show seemingly contradictory behavior — positive and negative Poisson's ratio, by applying different strain rates [66,67]. Moreover, the rate-dependent buckling behavior facilitates controlling the buckling pattern via different loading velocities. For instance, a study by Slesarenko and Rudykh [48] demonstrated that the buckling pattern of viscoelastic laminates could be modified by altering the compression velocities. Additionally, the properties of the soft metamaterials can be regulated by their viscoelasticity, which in turn, can be tuned, for example, by adjusting light intensity and other parameters during the photo-polymerization [51,68]. These effects can be combined with other external stimuli, such as electric [69,70], magnetic [71–78], and thermal loading [79,80] to control material dynamic behavior.

In this study, the simulations are performed in the 2D setting, therefore the conclusions may not be directly projected to composites with more diverse microstructures, and inclusion shapes and sizes. As the computational analysis is expanded to more realistic 3D settings, the utilization of computationally effective methods should be employed. For example, the application of the Local Background Grid method [81,82] has the potential to accommodate a broader range of inclusion types and provide a more accurate representation of their influence on the mechanical behavior of the composite. In this context, the exploration of deep learning methods presents a promising avenue for the efficient prediction of the mechanical response of viscoelastic composites [83,84]. Moreover, as the focus narrows to the microscale, the role of weak interparticle interactions, such as, van der Waals forces, hydrogen bonding, and electrostatic interactions increases [85,86]. In addition, we note that, while we study the most relevant mode (for buckling consideration) of global deformation – the compressive strain aligned with the inclusion column direction – composites may experience other, more complex deformation modes.

Table A.1
The material parameters for TangoPlus.

Branch (m)	β_m	τ_m (Unit: s)	Branch (m)	β_m	τ_m (Unit: s)
1	733.73	9.35E−11	6	210.28	3.60E−05
2	779.24	4.38E−09	7	40.60	2.37E−04
3	771.50	8.26E−08	8	7.05	0.0017
4	626.76	9.10E−07	9	1.96	0.016
5	426.89	6.50E−06	10	0.65	0.25
μ_∞ (MPa)	0.1633				

Declaration of competing interest

The authors declare that they have no known competing financial interests or personal relationships that could have appeared to influence the work reported in this paper.

Data availability

Data will be made available on request

Acknowledgments

The support from the University of Wisconsin–Madison with funding from the Wisconsin Alumni Research Foundation is gratefully acknowledged. SR acknowledges the support of the European Research Council (ERC) through Grant No. 852281- MAGIC.

Appendix. The parameters extraction for TangoPlus

We extract the 3D printed matrix material (Tangoplus) parameters by fitting the DMA data from Yuan et al. [54]. The fitting results are shown in Fig. A.1. The markers and dashed curves represent the experimental data and fitting results, respectively. The extracted strain-energy factors and relaxation times under room temperature (21 °C) are listed in Table A.1.

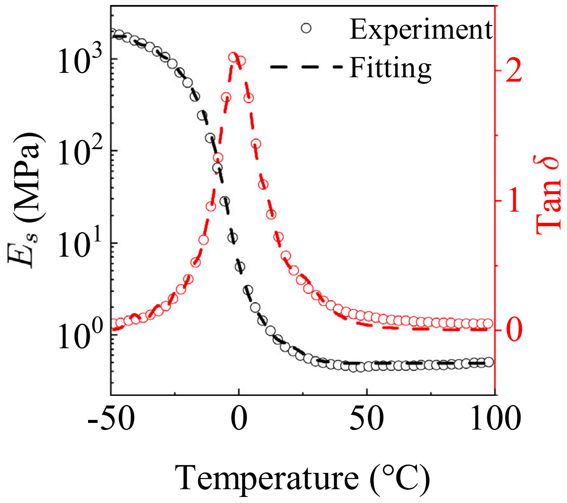

Fig. A.1. Fitting curves of the DMA results for TangoPlus.
Source: The data are extracted from Yuan et al. [54].

References

[1] Li J, Arora N, Rudykh S. Elastic instabilities, microstructure transformations, and pattern formations in soft materials. Curr Opin Solid State Mater Sci 2021;25(2):100898.

[2] Bertoldi K, Reis PM, Willshaw S, Mullin T. Negative Poisson's ratio behavior induced by an elastic instability. Adv Mater 2010;22(3):361–6.

[3] Li J, Slesarenko V, Rudykh S. Auxetic multiphase soft composite material design through instabilities with application for acoustic metamaterials. Soft Matter 2018;14(30):6171–80.

[4] Mullin T, Deschanel S, Bertoldi K, Boyce MC. Pattern transformation triggered by deformation. Phys Rev Lett 2007;99(8):084301.

[5] Bertoldi K, Vitelli V, Christensen J, Van Hecke M. Flexible mechanical metamaterials. Nat Rev Mater 2017;2(11):1–11.

[6] Li J, Shim J, Deng J, Overvelde JT, Zhu X, Bertoldi K, Yang S. Switching periodic membranes via pattern transformation and shape memory effect. Soft Matter 2012;8(40):10322–8.

[7] Li J, Slesarenko V, Rudykh S. Microscopic instabilities and elastic wave propagation in finitely deformed laminates with compressible hyperelastic phases. Eur J Mech A Solids 2019;73:126–36.

[8] Wang P, Casadei F, Shan S, Weaver JC, Bertoldi K. Harnessing buckling to design tunable locally resonant acoustic metamaterials. Phys Rev Lett 2014;113(1):014301.

[9] Pranno A, Greco F, Leonetti L, Lonetti P, Luciano R, De Maio U. Band gap tuning through microscopic instabilities of compressively loaded lightened nacre-like composite metamaterials. Compos Struct 2022;282:115032.

[10] Rafsanjani A, Bertoldi K, Studart AR. Programming soft robots with flexible mechanical metamaterials. Science Robotics 2019;4(29):eaav7874.

[11] Ogden RW. Non-linear elastic deformations. Dover civil and mechanical engineering, Dover Publications; 1997.

[12] Geymonat G, Müller S, Triantafyllidis N. Homogenization of nonlinearly elastic materials, microscopic bifurcation and macroscopic loss of rank-one convexity. Arch Ration Mech Anal 1993;122(3):231–90.

[13] Greco F, Leonetti L, De Maio U, Rudykh S, Pranno A. Macro-and micro-instabilities in incompressible bioinspired composite materials with nacre-like microstructure. Compos Struct 2021;269:114004.

[14] Greco F, Luciano R. A theoretical and numerical stability analysis for composite micro-structures by using homogenization theory. Composites B 2011;42(3):382–401.

[15] Rudykh S, Debotton G. Instabilities of hyperelastic fiber composites: micromechanical versus numerical analyses. J Elasticity 2012;106(2):123–47.

[16] Greco F, Lonetti P, Luciano R, Blasi PN, Pranno A. Nonlinear effects in fracture induced failure of compressively loaded fiber reinforced composites. Compos Struct 2018;189:688–99.

[17] Greco F, Leonetti L, Medaglia CM, Penna R, Pranno A. Nonlinear compressive failure analysis of biaxially loaded fiber reinforced materials. Composites B 2018;147:240–51.

[18] Merodio J, Ogden RW. Material instabilities in fiber-reinforced nonlinearly elastic solids under plane deformation. Arch Mech 2002;54(5–6):525–52.

[19] Merodio J, Ogden RW. Instabilities and loss of ellipticity in fiber-reinforced compressible non-linearly elastic solids under plane deformation. Int J Solids Struct 2003;40(18):4707–27.

[20] Merodio J, Ogden RW. Remarks on instabilities and ellipticity for a fiber-reinforced compressible nonlinearly elastic solid under plane deformation. Quart Appl Math 2005;63(2):325–33.

[21] Merodio J, Ogden RW. Tensile instabilities and ellipticity in fiber-reinforced compressible non-linearly elastic solids. Internat J Engrg Sci 2005;43(8–9):697–706.

[22] Merodio J, Pence TJ. Kink surfaces in a directionally reinforced neo-Hookean material under plane deformation: I. Mechanical equilibrium. J Elasticity 2001;62(2):119–44.

[23] Merodio J, Pence TJ. Kink surfaces in a directionally reinforced neo-Hookean material under plane deformation: II. Kink band stability and maximally dissipative band broadening. J Elasticity 2001;62:145–70.

[24] Qiu G, Pence T. Loss of ellipticity in plane deformation of a simple directionally reinforced incompressible nonlinearly elastic solid. J Elasticity 1997;49:31–63.

[25] Volokh K. Loss of ellipticity in elasticity with energy limiters. Eur J Mech A Solids 2017;63:36–42.

[26] Ehret AE, Itskov M. A polyconvex hyperelastic model for fiber-reinforced materials in application to soft tissues. J Mater Sci 2007;42:8853–63.

[27] Triantafyllidis N, Nestorović M, Schraad M. Failure surfaces for finitely strained two-phase periodic solids under general in-plane loading. J Appl Mech 2005;73(3):505–15.

[28] Lopez-Pamies O, Castañeda PP. On the overall behavior, microstructure evolution, and macroscopic stability in reinforced rubbers at large deformations: II—application to cylindrical fibers. J Mech Phys Solids 2006;54(4):831–63.

[29] Li J, Pallicity TD, Slesarenko V, Goshkoderia A, Rudykh S. Domain formations and pattern transitions via instabilities in soft heterogeneous materials. Adv Mater 2019;31(14):1807309.

[30] Chen D, Arora N, Xiang Y, Li J, Slesarenko V, Rudykh S. Instability-induced patterns and their post-buckling development in soft particulate composites. Mech Mater 2022;175:104482.

[31] Chen D, Xiang Y, Arora N, Yao Q, Li J, Rudykh S. Post-buckling development in soft particulate composites. Compos Struct 2023.

[32] Arora N, Batan A, Li J, Slesarenko V, Rudykh S. On the influence of inhomogeneous interphase layers on instabilities in hyperelastic composites. Materials 2019;12(5):763.

[33] Li J, Slesarenko V, Rudykh S. Emergence of instability-driven domains in soft stratified materials. Npj Comput Mater 2022;8(1):1–6.

[34] Arora N, Li J, Rudykh S. Tunable buckling configurations via in-plane periodicity in soft 3D-fiber composites: Simulations and experiments. Int J Solids Struct 2022;250:111711.

[35] Galich PI, Slesarenko V, Li J, Rudykh S. Elastic instabilities and shear waves in hyperelastic composites with various periodic fiber arrangements. Internat J Engrg Sci 2018;130:51–61.

[36] Li J, Slesarenko V, Galich PI, Rudykh S. Instabilities and pattern formations in 3D-printed deformable fiber composites. Composites B 2018;148:114–22.

[37] Slesarenko V, Rudykh S. Microscopic and macroscopic instabilities in hyperelastic fiber composites. J Mech Phys Solids 2017;99:471–82.

[38] Aboudi J, Gilat R. Bifurcation buckling and the effect of imperfections on the microbuckling of soft materials with periodic microstructure by the finite strain HFGMC micromechanics. Int J Solids Struct 2023;270:112227.

[39] Lakes R. Viscoelastic materials. Cambridge University Press; 2009.

[40] Aboudi J, Volokh KY. Modeling deformation and failure of viscoelastic composites at finite strains. Mech Soft Mater 2020;2:1–19.

[41] Xiang Y, Zhong D, Wang P, Yin T, Zhou H, Yu H, Baliga C, Qu S, Yang W. A physically based visco-hyperelastic constitutive model for soft materials. J Mech Phys Solids 2019;128:208–18.

[42] Arash B, Exner W, Rolfes R. Viscoelastic damage behavior of fiber reinforced nanoparticle-filled epoxy nanocomposites: multiscale modeling and experimental validation. In: Acting principles of nano-scaled matrix additives for composite structures. Springer; 2021, p. 377–410.

[43] Wang J, Peng X, Huang Z, Zhou H. A temperature-dependent 3D anisotropic visco-hyperelastic constitutive model for jute woven fabric reinforced poly (butylene succinate) biocomposite in thermoforming. Composites B 2021;208:108584.

[44] Andriß C, Kenf A, Schmeer S. Experimental characterization and phenomenological modeling of nonlinear viscoelasticity, plasticity and damage of continuous carbon fiber-reinforced thermoplastics. Composites B 2023;259:110734.

[45] Wineman A. Nonlinear viscoelastic solids—A review. Math Mech Solids 2009;14(3):300–66.

[46] Xiang Y, Zhong D, Rudykh S, Zhou H, Qu S, Yang W. A review of physically based and thermodynamically based constitutive models for soft materials. J Appl Mech 2020;87(11):110801.

[47] Alur K, Meaud J. Nonlinear mechanics of non-dilute viscoelastic layered composites. Int J Solids Struct 2015;72:130–43.

[48] Slesarenko V, Rudykh S. Harnessing viscoelasticity and instabilities for tuning wavy patterns in soft layered composites. Soft Matter 2016;12(16):3677–82.

[49] Holzapfel GA. On large strain viscoelasticity: continuum formulation and finite element applications to elastomeric structures. Internat J Numer Methods Engrg 1996;39(22):3903–26.

[50] Slesarenko V, Rudykh S. Towards mechanical characterization of soft digital materials for multimaterial 3D-printing. Internat J Engrg Sci 2018;123:62–72.

[51] Wu J, Zhao Z, Hamel CM, Mu X, Kuang X, Guo Z, Qi HJ. Evolution of material properties during free radical photopolymerization. J Mech Phys Solids 2018;112:25–49.

[52] Yu K, McClung AJ, Tandon GP, Baur JW, Jerry Qi H. A thermomechanical constitutive model for an epoxy based shape memory polymer and its parameter identifications. Mech Time-Depen Mater 2014;18(2):453–74.

[53] Suarez-Afanador C, Cornaggia R, Lahellec N, Maurel-Pantel A, Boussaa D, Moulinec H, Bordas SP-A. Effective thermo-viscoelastic behavior of short fiber reinforced thermo-rheologically simple polymers: An application to high temperature fiber reinforced additive manufacturing. Eur J Mech A Solids 2022;96:104701.

[54] Yuan C, Wang F, Qi B, Ding Z, Rosen DW, Ge Q. 3D printing of multi-material composites with tunable shape memory behavior. Mater Des 2020;193:108785.

[55] Lavoie SR, Millereau P, Creton C, Long R, Tang T. A continuum model for progressive damage in tough multinetwork elastomers. J Mech Phys Solids 2019;125:523–49.

[56] Zhong D, Xiang Y, Yin T, Yu H, Qu S, Yang W. A physically-based damage model for soft elastomeric materials with anisotropic mullins effect. Int J Solids Struct 2019;176:121–34.

[57] Suarez C, Cornaggia R, Maurel-Pantel A, Lahellec N, Boussa D, Moulinec H, Billon N, Bordas SP. Estimation du comportement thermo-viscoélastique effectif des pièces composites obtenues par impression 3D-FDM. In: Fabrication additive des composites (FabAddComp), AMAC, journées scientifiques et techniques. 2020.

[58] Hauseux P, Hale JS, Bordas SP. Accelerating Monte Carlo estimation with derivatives of high-level finite element models. Comput Methods Appl Mech Engrg 2017;318:917–36.

[59] Hauseux P, Hale JS, Cotin S, Bordas SP. Quantifying the uncertainty in a hyperelastic soft tissue model with stochastic parameters. Appl Math Model 2018;62:86–102.

[60] Rappel H, Beex LA, Noels L, Bordas S. Identifying elastoplastic parameters with Bayes' theorem considering output error, input error and model uncertainty. Probab Eng Mech 2019;55:28–41.

[61] Chen L, Lian H, Liu Z, Chen H, Atroshchenko E, Bordas S. Structural shape optimization of three dimensional acoustic problems with isogeometric boundary element methods. Comput Methods Appl Mech Engrg 2019;355:926–51.

[62] Ding C, Deokar RR, Ding Y, Li G, Cui X, Tamma KK, Bordas SP. Model order reduction accelerated Monte Carlo stochastic isogeometric method for the analysis of structures with high-dimensional and independent material uncertainties. Comput Methods Appl Mech Engrg 2019;349:266–84.

[63] Yu P, Bordas SPA, Kerfriden P. Adaptive isogeometric analysis for transient dynamics: Space-time refinement based on hierarchical a-posteriori error estimations. Comput Methods Appl Mech Engrg 2022;394:114774.

[64] Elouneg A, Sutula D, Chambert J, Lejeune A, Bordas S, Jacquet E. An open-source FEniCS-based framework for hyperelastic parameter estimation from noisy full-field data: Application to heterogeneous soft tissues. Comput Struct 2021;255:106620.

[65] Mazier A, Bilger A, Forte AE, Peterlik I, Hale JS, Bordas S. Inverse deformation analysis: an experimental and numerical assessment using the FEniCS project. Eng Comput 2022;38:4099–113.

[66] Bossart A, Dykstra DM, Van der Laan J, Coulais C. Oligomodal metamaterials with multifunctional mechanics. Proc Natl Acad Sci 2021;118(21):e2018610118.

[67] Janbaz S, Narooei K, Van Manen T, Zadpoor A. Strain rate–dependent mechanical metamaterials. Sci Adv 2020;6(25):eaba0616.

[68] Xiang Y, Schilling C, Arora N, Boydston A, Rudykh S. Mechanical characterization and constitutive modeling of visco- hyperelasticity of photocured polymers. Addit Manuf 2020;36:101511.

[69] Rudykh S, Bhattacharya K, deBotton G. Snap-through actuation of thick-wall electroactive balloons. Int J Non-Linear Mech 2012;47(2):206–9.

[70] Acome E, Mitchell SK, Morrissey T, Emmett M, Benjamin C, King M, Radakovitz M, Keplinger C. Hydraulically amplified self-healing electrostatic actuators with muscle-like performance. Science 2018;359(6371):61–5.

[71] Goshkoderia A, Chen V, Li J, Juhl A, Buskohl P, Rudykh S. Instability-induced pattern formations in soft magnetoactive composites. Phys Rev Lett 2020;124(15):158002.

[72] Pathak P, Arora N, Rudykh S. Magnetoelastic instabilities in soft laminates with ferromagnetic hyperelastic phases. Int J Mech Sci 2022;213:106862.

[73] Rudykh S, Bertoldi K. Stability of anisotropic magnetorheological elastomers in finite deformations: A micromechanical approach. J Mech Phys Solids 2013;61(4):949–67.

[74] Chen VW, Arora N, Goshkoderia A, Willey CL, Turgut Z, Buskohl PR, Rudykh S, Juhl AT. Mechanical instability tuning of a magnetorheological elastomer composite laminate. Composites B 2023;251:110472.

[75] Garcia-Gonzalez D, Ter-Yesayants T, Moreno-Mateos MA, Lopez-Donaire ML. Hard-magnetic phenomena enable autonomous self-healing elastomers. Composites B 2023;248:110357.

[76] Moreno M, Gonzalez-Rico J, Lopez-Donaire M, Arias A, Garcia-Gonzalez D. New experimental insights into magneto-mechanical rate dependences of magnetorheological elastomers. Composites B 2021;224:109148.

[77] Zhang Q, Rudykh S. Magneto-deformation and transverse elastic waves in hard-magnetic soft laminates. Mech Mater 2022;169:104325.

[78] Garcia-Gonzalez D, Moreno M, Valencia L, Arias A, Velasco D. Influence of elastomeric matrix and particle volume fraction on the mechanical response of magneto-active polymers. Composites B 2021;215:108796.

[79] Che K, Rouleau M, Meaud J. Temperature-tunable time-dependent snapping of viscoelastic metastructures with snap-through instabilities. Extreme Mech Lett 2019;32:100528.

[80] Yuan C, Mu X, Dunn CK, Haidar J, Wang T, Jerry Qi H. Thermomechanically triggered two-stage pattern switching of 2D lattices for adaptive structures. Adv Funct Mater 2018;28(18):1705727.

[81] Ouyang H, Chen X. 3D meso-scale modeling of concrete with a local background grid method. Constr Build Mater 2020;257:119382.

[82] Yu P, Ren Z, Chen Z, Bordas SPA. A multiscale finite element model for prediction of tensile strength of concrete. Finite Elem Anal Des 2023;215:103877.

[83] Krokos V, Bui Xuan V, Bordas SP, Young P, Kerfriden P. A Bayesian multiscale CNN framework to predict local stress fields in structures with microscale features. Comput Mech 2022;69(3):733–66.

[84] Deshpande S, Lengiewicz J, Bordas SP. Probabilistic deep learning for real-time large deformation simulations. Comput Methods Appl Mech Engrg 2022;398:115307.

[85] Hauseux P, Ambrosetti A, Bordas SP, Tkatchenko A. Colossal enhancement of atomic force response in van der Waals materials arising from many-body electronic correlations. Phys Rev Lett 2022;128(10):106101.

[86] Budarapu PR, Zhuang X, Rabczuk T, Bordas SP. Multiscale modeling of material failure: Theory and computational methods. Adv Appl Mech 2019;52:1–103.